Theoretical and experimental studies of double-unit air gap membrane distillation (DUAGMD) module for seawater desalination

Chii-Dong Ho[a,*], Luke Chen[b], Yu-An Chen[a], Jia-Yu Jiang[a], Pin-Tsen Lu[b]

[a]*Chemical and Materials Engineering Department, Tamkang University, Tamsui, New Taipei 251, Taiwan,
Tel. +886-2-26215656-2724; emails: cdho@mail.tku.edu.tw (C.-D. Ho), yuan53049@gmail.com (Y.-A. Chen),
a0955203250@gmail.com (J.-Y. Jiang)*
[b]*Water Resources and Environmental Engineering Department, Tamkang University, Tamsui, New Taipei 251, Taiwan,
emails: luke@mail.tku.edu.tw (L. Chen), polar87216@gmail.com (P.-T. Lu)*

ABSTRACT

This study proposes modeling techniques for predicting distillate flux in a double-unit air gap membrane distillation (DUAGMD) module. The prediction is validated by experimental results by inserting S-ribs carbon-fiber spacers acting as an eddy promoter. A more compact double-unit device implementing S-ribs carbon-fiber spacers could increase the membrane stability to prevent flow-induced vibration and also enhance the production rate by suppressing temperature polarization on the membrane surface. The new design achieves a considerable pure water productivity by inserting S-ribs carbon-fiber spacers in the saline feed channel compared to an empty channel and the single unit module. The formulated Nusselt numbers are regressed with experimental data to predict the heat transfer coefficient of the DUAGMD module for both S-ribs carbon-fiber filled and empty channels. This study contributes to summarizing the effects of volumetric flow rate, saline feed temperature, and S-ribs types on the permeate flux. Besides analyzing the permeate flux enhancement, this study compares the energy consumption increment caused by the S-ribs carbon-fiber filled design with the permeate flux increment. A nice consistency between the experimental results and theoretical predictions has shown that the proposed model could predict AGMD system's design and optimize the operation parameters.

Keywords: Air gap membrane distillation; Double-unit module; Permeate flux; S-ribs carbon-fiber spacers; Temperature polarization.

1. Introduction

Membrane distillation (MD) is a non-isothermal desalination technology for desalination, solution concentration, and wastewater treatment [1] because of its simplicity and low-energy requirements compared to another thermal desalination process [2,3]. A trans-membrane temperature gradient builds up the vapor pressure difference across the hydrophobic microporous membrane to generate vapor flux from the feed side to the permeate side in the MD process [4]. There are four MD systems commonly investigated, namely the direct contact MD (DCMD), air gap MD (AGMD), sweep gap MD (SGMD), and vacuum MD (VMD). Among the four configurations of MD, the air gap membrane distillation (AGMD) has considerably more energy efficiency and the most versatile configuration [5]. In addition to the four MD systems, some derived MD systems, including liquid or water gap MD (LGMD/WGMD), thermostatic SGMD (TSGMD), and vacuum assist AGMD (VA-AGMD) were evaluated and compared for their features and performance [6]. The evaluation concluded that temperature and concentration polarization effects had been identified as significant limits for the MD flux performance, which are the major factors for assessing MD

---

* Corresponding author.

application at the industrial scale. Detailed modeling studies are required to help identify and simulate the magnitude of these effects on the MD system.

Various approaches such as spacers [7], filament [8] and roughened surface [9] proposed to reduce the temperature polarization effect would be to use eddy promoters in the flow channel what aims at decreasing the thermal boundary-layer thickness and leading to the heat and mass transfer enhancement. Previous investigations of the flux improvement under more insight based on mathematical models were achieved by using computational fluid dynamics (CFD) [10,11]. The heat and mass transport modeling approaches usually applied in membrane distillation were reviewed by Dong [12]. Ongoing research in AGMD involves vacuum AGMD integrated module [13], spiral wound configuration [14], eddy promoter in flow channel [15], and porous and non-porous hollow fiber module [16], as well as the improvement in its lower permeate flux. The performance of the multi-stages MD system was compared with single-stage MD system [17]. The specific thermal consumption of the MD system was also

compared for multi-stage with single-stage VMD systems [18]. To improve the design and the performance of AGMD system, we proposed a compact DUAGMD system that is investigated experimentally and theoretically. The enhanced plate-type double-unit AGMD module (DUAGMD) filled with S-ribs carbon fiber spacers in the further compact implementation with its performance was studied experimentally and numerically. The DUAGMD module built with a self-supporting hydrophobic membrane can provide a compact volume with double membrane surface per unit equipment. However, the pressure drops with power consumption increments introduced by implementing eddy promoters in the flow channel had been taken into consideration, and the economic analysis is conducted [19].

This study aims to formulate a theoretical model for the DUAGMD module to predict the module's permeate fluxes and analyze the module's energy efficiency. A correlated equation of the heat-transfer enhancement factor referred as Reynolds number using the S-ribs carbon-fiber-filled channel was developed and validated with experiments. The trade-off judgment between DUAGMD productivity
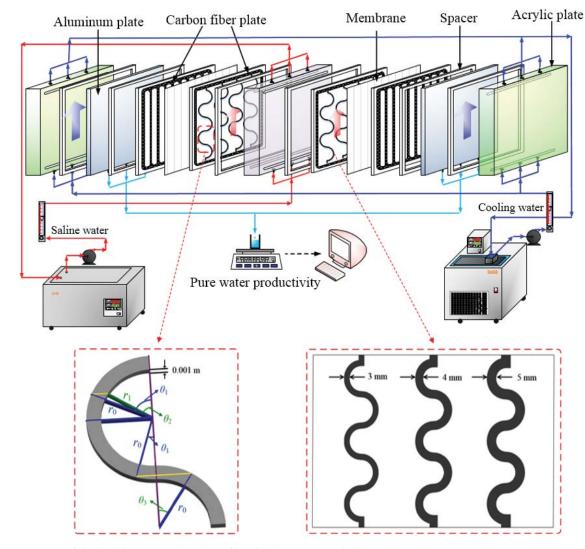

Fig. 1. Components of the double-unit S-ribs carbon-fiber filled AGMD module.

increment and the corresponding power consumption increment due to the eddy promoter was also analyzed.

2. Model description

A new design of a double-unit AGMD module for pure water production is comprised of double units of evaporating and condensing sides, as shown in Fig. 1. The permeate water is vaporized at the membrane-liquid interfaces of the hot feed side and transported through porous hydrophobic membranes. And the water vapor is finally condensed on the cold side plate surface to complete the distillate process. Therefore, a similar theoretical model and boundary conditions for a single unit AGMD module can be applied for each unit in the DUAGMD module. Such model demonstrates a single AGMD unit conjugated with the other one in this study. At the same time, the theoretical analysis of the DUAGMD is similar to the mathematical formulation generated in our existing research contribution of a single AGMD unit [20]. The assumptions were made to develop the theoretical model of the module as follows:

(a) Under steady-state operations;
(b) Physical properties of fluid, plates and membrane are constants;
(c) Stagnant air within the membrane pore;
(d) The condensate forms a thin liquid film and covers the entire condensing surface;
(e) Mass transfer by diffusion and heat transfer by conduction within the air gap;
(f) No water passing through the hydrophobic membrane;
(g) Well insulation on the bottom and edge sides of modules.

2.1. Mass transfer

Based on the mean free path of water molecules and the membrane pore size, the dusty-gas model states that the permeate flux of water vapor across a porous medium can be evaluated using a membrane permeation coefficient (c_m). The trans-membrane saturation vapor pressure difference (ΔP). The membrane permeation coefficient is the addition of Knudsen diffusion and Poiseuille flow [21,22]:

$$N_m'' = c_m \Delta P = c_m \left[P_1^{sat}(T_1) - P_2^{sat}(T_2) \right] \tag{1}$$

where

$$c_m = \left(\frac{1}{c_K} + \frac{1}{c_M} \right)^{-1} = \left\{ \left[1.064 \frac{\varepsilon r}{\tau \delta_m} \left(\frac{M_w}{RT_m} \right)^{1/2} \right]^{-1} + \left[\frac{1}{|Y_m|_{ln}} \frac{D_m \varepsilon}{\delta_m \tau} \frac{M_w}{RT_m} \right]^{-1} \right\}^{-1} \tag{2}$$

the hot feed side saturation vapor pressure (P_1^{sat}) can be estimated using water activity coefficient (a_w), which is determined below [4]:

$$P_1^{sat} = y_w P = x_w a_w P_w^{sat} \tag{3}$$

$$a_w = 1 - 0.5 x_{NaCl} - 10 x_{NaCl}^2 \tag{4}$$

and the tortuosity (τ) was estimated by the porosity of the membrane [23].

$$\tau = \frac{1}{\varepsilon} \tag{5}$$

The amount of the molar vapor flux diffusing through a stagnant air film over the air gap layer by molecular diffusion [24] was expressed as:

$$N_a'' = c_a \left[P_2^{sat}(T_2) - P_3^{sat}(T_3) \right] \tag{6}$$

The total vapor permeate flux was calculated by equating the permeate fluxes in the membrane and air gap, Eqs. (1) and (6), with the total mass-transfer resistances:

$$N'' = N_a'' = N_m'' = c_T \left[P_1^{sat}(T_1) - P_3^{sat}(T_3) \right] \tag{7}$$

in which

$$c_T = \left(\frac{1}{c_m} + \frac{1}{c_a} \right)^{-1} \tag{8}$$

2.2. Heat transfer

To calculate vapor permeate flux, the temperatures of membrane surfaces on both feed and permeate sides must be given. To obtain the membrane surface temperatures, we proposed a model to simulate a non-isothermal process with the energy balance of enthalpy flow of the conventional AGMD system. As the given temperature gradient across the whole module resulting in heat transfer was calculated, the vapor permeates flux can then be predicted with the mass transfer model mentioned earlier. Heat transfer in the DUAGMD system caused by the temperature gradient across each component of the module is illustrated in Fig. 2. For a single-unit AGMD in each heat transfer region (1) the hot feed stream, (2) hydrophobic membrane, (3) air gap, (4) cooling plate, and (5) cooling water under the steady-state operation may be derived by balancing energy in each component. The thermal boundary layers of both water and air channels play an essential role in determining the permeate flux and represent the magnitude of heat transfer resistance in each fluid side, which is commonly expressed as the temperature polarization coefficient (τ_{temp}) defined below:

$$\tau_{temp} = \frac{(T_1 - T_3)}{(T_h - T_c)} \tag{9}$$

A higher value of τ_{temp} indicates lower thermal boundary-layer resistances, and the temperature polarization coefficient can be expressed in terms of heat transfer resistances in series as follows.

Equating the energy conservation of heat fluxes in each region for two intervals, $(T_1 - T_3)$ and $(T_3 - T_c)$ as shown in Fig. 3, with good insulation on the bottom and edge sides of modules leads to the overall heat transfer coefficient of the hot feed stream and cooling stream, respectively.

$$q'' = q''_{ma} = q''_m + q''_a = \left\{ \left(\frac{k_m}{\delta_m} + \frac{k_a}{\delta_a} \right)^{-1} + \left[c_T \frac{\left((1-x_{NaCl})(1-0.5x_{NaCl}-10x_{NaCl}^2)P_w^{sat} + P_3^{sat} \right)\lambda^2 M_w}{2RT_{avg}^2} \right] \right\} (T_1 - T_3) = H_m (T_1 - T_3) \qquad (10)$$

and

$$q''_{fc} = \frac{1}{1/h_f + \delta_p/k_p + 1/h_c}(T_3 - T_c) = H_c(T_3 - T_c) \qquad (11)$$

in which the heat fluxes transferred through the thermal boundary layers in both fluid channels to and from the membrane surfaces with neglecting the net enthalpy flow due to the temperature gradient can be determined by convective heat-transfer coefficients and expressed as:

$$q''_h = h_h(T_h - T_1), \text{ the hot feed water region} \qquad (12)$$

$$q''_c = h_c(T_5 - T_c), \text{ the cooling water region} \qquad (13)$$

$$q''_m = \frac{k_m}{\delta_m}(T_1 - T_2) + N''\lambda, \text{ the membrane region} \qquad (14)$$

$$q''_a = \frac{k_a}{\delta_a}(T_2 - T_3) + N''\lambda, \text{ the air gap region} \qquad (15)$$

$$q''_f = h_f(T_3 - T_4) = 0.943 \left[\frac{\rho^2 g\lambda k_f^3}{\mu L(T_3 - T_4)} \right]^{\frac{1}{4}} (T_3 - T_4),$$
$$\text{the condensate film} \qquad (16)$$

$$q''_p = \frac{k_p}{\delta_p}(T_4 - T_5), \text{ the condensing plate} \qquad (17)$$

where the heat transfer coefficient for the condensate film in Eq. (16) was found by Banat and Simandl [25], and the thermal conductivity of the membrane was assumed by Warner [26] as:

$$k_m = \varepsilon k_g + (1-\varepsilon)k_s \qquad (18)$$

Combinations of Eqs. (10) and (11) and Eqs. (10) and (12) yield the bulk temperatures of both hot and cold streams, respectively:

$$T_c = T_3 - \frac{H_m}{H_c}(T_1 - T_3) \qquad (19)$$

$$T_h = T_1 + \frac{H_m}{h_h}(T_1 - T_3) \qquad (20)$$

The membrane surface temperature T_1 on hot feed side and the temperature on condensate film T_3 are obtained by rearranging Eqs. (19) and (20) as:

$$T_1 = \frac{h_h T_h + H_m T_3}{h_h + H_m} \qquad (21)$$
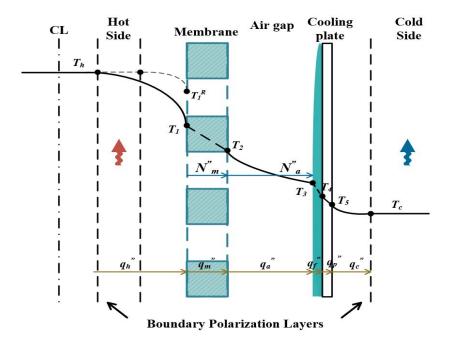

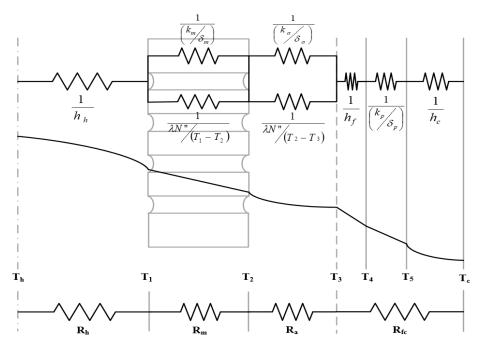Fig. 2. Schematic of mass and heat transfer through the DUAGMD module.

Fig. 3. Mass and heat transfer resistances in the DUAGMD module.

$$T_3 = \frac{H_c T_c + H_m T_1}{H_c + H_m} \tag{22}$$

Substituting Eqs. (19)–(22) into Eq. (9) gives the temperature polarization coefficient τ_{temp} in terms of heat transfer coefficients as:

$$\tau_{\text{temp}} = \frac{h_h H_c}{h_h H_c + h_h H_m + H_c H_m} \tag{23}$$

The one-dimensional governing equations for temperature variation of both hot feed and cold bulk streams along the flow direction, as illustrated in Fig. 4, were derived by energy conservation as:

$$\frac{dT_h}{dz} = \frac{-Q_h W_h}{\dot{m}_h C_{p,h}} \tag{24}$$

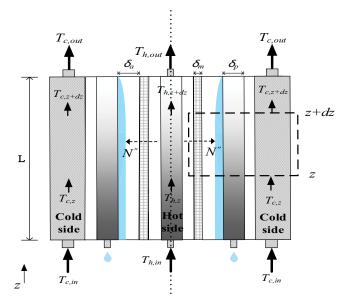$$\frac{dT_c}{dz} = \frac{Q_c W_c}{\dot{m}_c C_{p,c}} \tag{25}$$

where z is the coordinate in the flow direction, and W_h and W_c represent the channel width of the hot and cold channels, respectively. The flow channel of double-unit AGMD modules inserted the S-ribs carbon-fiber spacers were found to indicate the new spacers disrupt laminar boundary layer and enhance the local shear stress on the membrane surface owing to increasing hydrodynamic conditions, and to create more intensive vortices or secondary flow characteristics in mitigating temperature polarization effect, and thus, a higher permeate flux is achieved. Equations (24) and (25) could be rewritten in terms of the temperature

polarization coefficient τ_{temp} and the difference between the hot and cold streams with the use of Eqs. (9) and (10) as:

$$\frac{dT_h}{dz} = \frac{-W_h}{\dot{m}_h C_{p,h}} H_m \, \tau_{\text{temp}} \left(T_h - T_c \right) \tag{26}$$

$$\frac{dT_c}{dz} = \frac{W_c}{\dot{m}_c C_{p,c}} H_m \, \tau_{\text{temp}} \left(T_h - T_c \right) \tag{27}$$

Eqs. (26) and (27) are used for solving the bulk temperature distributions of both hot feed and cold streams by a fourth-order Runge–Kutta numerical method given the convective heat transfer coefficients h_h. The heat transfer rate depends on the convective heat-transfer coefficient and latent heat across the membrane, which were implicitly related to temperature polarization coefficient and incorporated into the energy balance equations of Eqs. (26) and (27) to solve the temperature fields. Computational fluid dynamics was commonly used to simulate the temperature field when combined with energy equation. However, if semi-empirical correlation equation was not proposed in the calculation procedure, one can't couple energy equation in CFD only to solve temperature field without the convective heat-transfer coefficient associated with latent heat. It was achieved by the turbulence intensity augmentation from inserting eddy promoters. Applying the semi-empirical correlation approach, one can solve the temperature field and quantify the enhanced permeate flux due to eddy promoter of the system directly. When CFD simulation is used in analyzing the system, one needs to specify boundary condition for latent heat on the membrane surface as energy sink where an empirical model is also required for the simulation. An iterative procedure, as illustrated

Fig. 4. Schematic representation of Double-Unit AGMD distillation module.

in Fig. 5, was conducted to obtain the h_h, membrane surface temperature T_1 on the hot feed side and the temperature on condensate film T_3. Hence the permeate flux can be predicted and correlated with experimental data. Da Costa et al. [19] suggested the enhancement factor for spacer-filled channels were correlated by multiple linear regressions to obtain the heat transfer correlation for spacer-filled channels and the further application was investigated by Phattaranawik et al. [27]. For the S-ribs carbon-fiber AGMD module, an enhancement factor was introduced as:

$$\alpha^s = \frac{Nu^s}{Nu_{lam}} \tag{28}$$

where

$$Nu^s = \frac{h_h De}{k}, \text{ S-ribs carbon-fiber filled channel module} \tag{29}$$

$$Nu_{lam} = 4.36 + \frac{0.036 \, Re \, Pr \, (De/L)}{1 + 0.011 \left(Re \, Pr \, (De/L) \right)^{0.8}}, \tag{30}$$
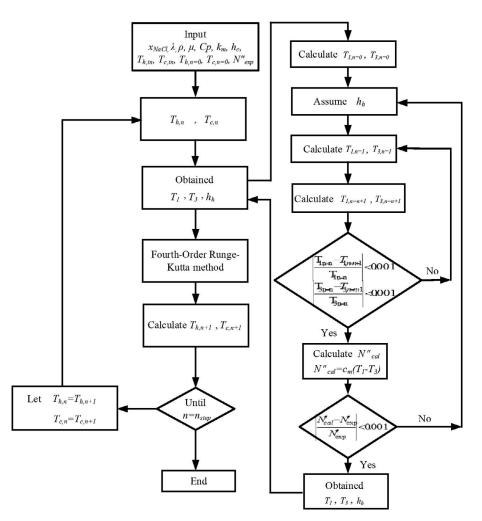
empty channel module

Fig. 5. Calculation flow chart for determining the heat transfer coefficients and the temperature distributions in hot feed and cold channels.

The filled S-ribs carbon-fiber spacers play a vital role as the eddy promoter in the channel flow. According to Buckingham's π theorem, the Nusselt number of channels with inserting S-ribs carbon-fiber spacers can be grouped into four dimensionless parameters:

$$Nu^s = f\left(\frac{A}{A_f}, \frac{De}{De_f}, Re, Pr\right) \tag{31}$$

where A and De are the cross-sectional area and equivalent diameter of channels with S-ribs carbon-fiber spacers, while A_f and De_f are the cross-sectional area and hydraulic diameter of the module with the empty channel.

The channel filled with S-ribs carbon-fiber spacers acting as eddy promoters consumes more power than the empty channel because more flow resistance was introduced. The power consumption of the DUAGMD module attributed to both the hot feed side and the cold fluid side can be determined using Fanning friction factor (f_F) [28]:

$$P = P_h + P_c = Q_h \rho_h \ell w_{f,h} + Q_c \rho_c \ell w_{f,c} \tag{32}$$

$$\ell w_{f,i} = \frac{2 f_{F,i} \bar{v}_i^2 L}{d_{h,i}}, i = h, c \tag{33}$$

in which

$$\bar{v}_h = \frac{Q_h}{(dW - D_1 W_1 N_1)}, \bar{v}_c = \frac{Q_c}{A} \tag{34}$$

$$d_{h,h} = \frac{4(dW - D_1 W_1 N_1)}{2(d + W + D_1 N_1)}, \quad d_{h,c} = \frac{4dW}{2(d + W)} \tag{35}$$

The Fanning friction factor can be estimated using a correlation based on the aspect ratio of the channel ($\alpha = d/W$) [29]:

$$f_{F,h} = \frac{C}{Re_h}, \quad f_{f,c} = \frac{C}{Re_c} \tag{36}$$

$$C = 24 \begin{pmatrix} 1 - 1.3553\,\alpha + 1.9467\,\alpha^2 - 1.7012\,\alpha^3 \\ + 0.9564\,\alpha^4 - 0.2537\alpha^5 \end{pmatrix} \tag{37}$$

The relative degree of permeate flux enhancement and power consumption increment, I_N and I_p are defined below.

$$I_N = \frac{N''_{spacer} - N''_{empty}}{N''_{empty}} \times 100\% \tag{38}$$

$$I_p = \frac{H_{spacer} - H_{empty}}{H_{empty}} \times 100\% \tag{39}$$

3. Module design and experimental apparatus

The schematic representation of the DUAGMD module is shown in Fig. 4 while the module units are assembled in a pattern that the hot-feed channels or cold-feed channels of two neighboring units are stacked together, as illustrated in Fig. 1. This device allows the elimination of a solid thermal insulation boundary between two adjacent single-unit modules. The hot-to-hot assembly makes a compact double-unit AGMD operation by inserting an aluminum plate between the two adjacent hot channels that have three holes flowing in and out at both entrance and exit ends. Thus, the corresponding membrane area can double under the same volumetric flow rate.

The experimental setup of the DUAGMD module with/without (empty channel) S-ribs carbon-fiber spacers is illustrated in Fig. 6, and a photo of the present experimental apparatus is shown in Fig. 7 with the acrylic plates as outside walls. The outside acrylic plates enclose the cold-feed channels having three holes on the top and bottom for cold fluid flowing in and out. A 2 mm silicon spacer separates two adjacent units with 2 mm thickness of air gap channel. Each hot and cold channel's length, width, and height are 0.21, 0.29, and 2 mm, respectively. The hydrophobic PTFE (polytetrafluoroethylene) membrane (ADVANTEC) with a nominal pore size of 0.2 μm, a porosity of 0.72, and a thickness of 130 μm was used. The conductance of the collected permeate flux was measured and less than 1.5 μs/cm. Two 1 mm-thick carbon fiber sheets with S-ribs carbon-fiber width of 3, 4, and 5 mm, respectively, were placed on both sides of the membrane, as shown in Fig. 6. The S-ribs carbon-fiber spacers serve for creating the fluid flow channel, equipping the mechanical strength of the units and acting as turbulence promoters. Between the aluminum plate or the acrylic plate and the S-ribs carbon-fiber spacers is a 1mm-thick silicon rubber sealing. The function of sealing silicon rubber plays dual roles in offering the flow channel and preventing leakage. Two parallel adjacent compartments hence make individual flow channel, one is the empty space created by the silicon rubber and the other is a channel filled with the S-ribs carbon-fiber spacers.

The hot feed saline water of 3.5 wt% NaCl was prepared using distilled water, and two thermostats were used to keep the inlet hot and cold water at specified temperatures, respectively. The trans-membrane water vapor reached and condensed at the thin aluminum plate, which was collected and weighted using an electronic balance. Each single unit of the DUAGMD module was operated under the same inlet flow rate controlled by conventional pumps. The experimental runs were carried out for different hot feed temperatures (40°C, 45°C, 50°C, and 55°C) and volumetric flow rates (0.3, 0.5, 0.7, and 0.9 L/min), while the cold water had a fixed inlet temperature of 25°C and specified volumetric flow rate of 0.9 L/min. Experiments were conducted for the modules with both empty channel and S-ribs carbon-fiber filled channel.

Moffat [30] determined the precision analysis of experimental uncertainty for each individual measurement from the experimental results as follows:

$$S_{N''_{exp}} = \left\{ \sum_{i=1}^{N_{exp}} \frac{\left(N''_{exp,i} - \overline{N''_{exp,i}}\right)^2}{N_{exp} - 1} \right\}^{1/2} \tag{40}$$

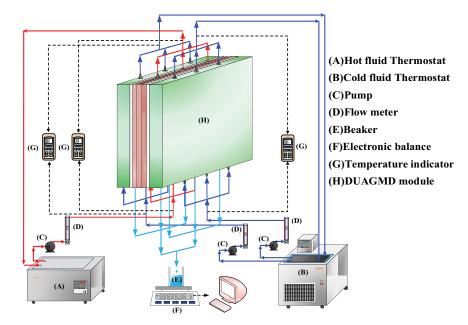The mean value of the resulting uncertainty of the experimental measurements was defined by:
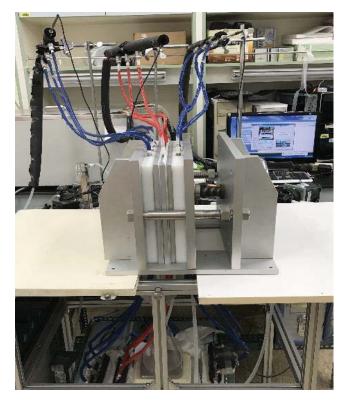
Fig. 6. Experimental setup of the DUAGMD system.

Fig. 7. A photo of the experimental apparatus of the DUAGMD system.

$$S_{\overline{N''_{\exp}}} = \frac{S_{N''_{\exp}}}{\sqrt{N_{\exp}}} \qquad (41)$$

The mean experimental uncertainty in Table ranges between $5.41 \times 10^{-3} \le S_{\overline{N''_{\exp}}} \le 9.36 \times 10^{-3}$. Meanwhile, the deviation of the experimental results from the theoretical predictions was calculated using the following definition as:

$$E = \frac{1}{N_{\exp}} \sum_{i=1}^{N_{\exp}} \frac{\left| N''_{\text{theo},i} - N''_{\exp,i} \right|}{N''_{\text{theo},i}} \qquad (42)$$

where $N_{\exp}$, $N''_{\exp,i}$ and $N''_{\text{theo},i}$ are the number of experimental runs, theoretical predictions and experimental results of collector efficiencies, respectively. The accuracy deviations with various carbon-fiber spacer widths was shown in Table 1. The deviation of experimental results from theoretical predictions is well minimized within $1.02 \times 10^{-2} \le E \le 9.94 \times 10^{-2}$.

4. Results and discussion

The temperature distributions along the module for hot feed and cold bulk flow and membrane surfaces can be solved numerically for concurrent operation, as illustrated in Fig. 8. Both hot feed and cold streams bulk temperatures converge toward downstream. And the higher flow rate results in the higher temperature gradient between the temperatures on hot feed side of membrane surface and the temperature on condensate surface, namely T_1 and T_3 respectively. The enlarged temperature gradient on both sides of the membrane surface enhances the vapor transport through the membrane. More distilled water condensed on a cold surface.

The temperature distributions further determines τ_{temp} as shown in Fig. 9. The modules with τ_{temp} values in descending order are S-ribs carbon-fiber filled channel with the width of 3 mm, 4 mm, and empty channel. Comparably, S-ribs carbon-fiber filled channel results in much higher τ_{temp} than that in the empty channel. Substantial increment in τ_{temp} for the S-ribs carbon-fiber filled channel versus the empty channel were observed. The enforcement in suppressing temperature

Table 1
The accuracy deviation between theoretical predictions and experimental results. $T_{c,in}$ = 25°C

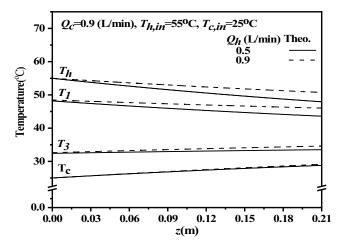| | | Saline water, NaCl = 3.5 wt% | | | | | | | | |
		3 mm			4 mm			5 mm		
$T_{h,in}$ (°C)	Q_h (L/min)	$N''_{s,exp}$	$N''_{s,theo}$	E	$N''_{s,exp}$	$N''_{s,theo}$	E	$N''_{s,exp}$	$N''_{s,theo}$	E
		(kg/m² h)	(kg/m² h)	100%	(kg/m² h)	(kg/m² h)	100%	(kg/m² h)	(kg/m² h)	100%
	0.3	1.402	1.538	8.8	1.395	1.524	8.5	1.368	1.513	9.68
40	0.5	1.716	1.869	8.2	1.694	1.846	8.2	1.682	1.832	8.2
	0.7	1.940	2.084	6.9	1.932	2.063	6.4	1.906	2.049	7.0
	0.9	2.318	2.230	4.0	2.240	2.195	2.1	2.219	2.177	1.9
45	0.3	1.920	2.132	9.9	1.918	2.098	8.6	1.894	2.082	9.0
	0.5	2.422	2.638	8.2	2.438	2.594	6.0	2.355	2.578	8.7
	0.7	2.767	2.920	5.2	2.769	2.874	3.7	2.913	2.848	2.3
	0.9	2.996	3.128	4.2	2.970	3.078	3.5	2.932	3.040	3.6
	0.3	2.485	2.684	7.4	2.456	2.656	7.5	2.436	2.624	7.2
50	0.5	3.146	3.381	7.0	3.108	3.325	6.5	3.083	3.290	6.3
	0.7	3.843	3.738	2.81	3.515	3.689	4.7	3.786	3.645	3.9
	0.9	4.108	4.065	1.1	4.104	3.998	2.7	4.062	3.943	3.0
55	0.3	3.115	3.352	7.1	3.065	3.317	7.6	3.057	3.283	6.9
	0.5	3.947	4.169	5.3	3.914	4.122	5.1	4.252	4.079	4.2
	0.7	4.492	4.634	3.1	4.686	4.571	2.5	4.570	4.524	1.0
	0.9	5.122	5.018	2.1	4.852	4.954	2.1	4.986	4.896	1.8

Fig. 8. Effect of feed flow rate on temperature distributions along the module.

polarization results from the filled S-ribs carbon-fiber spacers that serve as the role of a turbulence promoter to mitigate the heat transfer resistance to the thermal boundary layer on the membrane surface in hot saline feed channel.

When comparing the τ_{temp} values for different inlet hot feed temperatures, one may notice that the τ_{temp} values for hot feed temperature of 40°C are higher than that of 55°C. The higher hot feed temperature not giving higher τ_{temp} values means the thermal efficiency of the process decreases as the hot feed temperature increases. This is because the higher hot feed temperature does not reduce the heat transfer resistance built up in the thermal boundary layer on the

membrane surface of on the hot feed bulk flow. Therefore, the increased enthalpy caused by the raised hot feed temperature cannot be quickly delivered to the membrane surface accordingly. Comparing the difference in τ_{temp} between the S-ribs carbon-fiber filled channels with widths of 3 and 4 mm, respectively, one found that the τ_{temp} difference decreases with the inlet hot feed temperature and the S-ribs carbon-fiber spacer width, as shown in Fig. 9. The comparison confirms that the higher hot feed temperature results in the smaller thermal efficiency for all types of channel designs.

The heat transfer coefficients of hot saline feed, determined by the experimental results and the theoretical model, are compared to the correlation predictions in Fig. 10. The correlation of Nusselt number referred to empty channel is calculated by Eq. (30), while the correlation of Nusselt number for the S-ribs carbon-fiber filled channels is determined by Eq. (29) in terms of the enhancement factor α^s. The α^s determined via a regression analysis is:

$$\alpha^s = \frac{Nu^s}{Nu_{lam}} = 2.568 \exp\left(\frac{W_1}{d_h}\right)^{-0.140} \tag{43}$$

The squared correlation coefficient (R^2) of the regression is 0.95. The experimental results of Nu vs. Re for the empty channel and S-ribs carbon-fiber filled channels are presented in Fig. 11. The results indicated that the higher inlet saline feed temperature results in larger Nu numbers, and thus, a higher heat transfer was obtained. The Nu numbers predicted from Eq. (40) are pretty close to the experimental results of the empty channel. With the
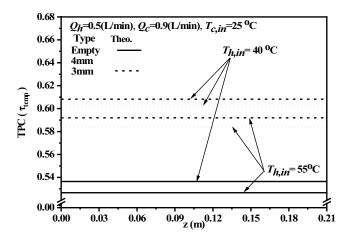
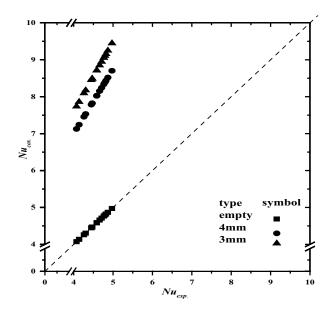Fig. 9. Effect of saline feed temperature and channel designs on τ_{temp}.

Fig. 10. Comparison of predicted and experimental Nusselt numbers for different channel designs.

Fig. 11. Dependence of Nu on Re for different channel designs and saline feed temperature.

predicted heat transfer coefficients for the empty channel and the S-ribs carbon-fiber filled channels, further prediction of permeate flux could be applicable for various channel designs.

The experimental results of permeate flux N'' and permeate flux enhancement I_N are summarized by Table 2. Compared to an empty channel, the S-ribs carbon-fiber filled channel of 3, 4, and 5 mm width spacer can provide a relative increase of permeate flux (I_N) of 8.46%–16.8%, 7.5%–15.3%, and 6.7%–14%, respectively. Fig. 12 shows that the consistency between the experimental results and theoretical predictions of permeate fluxes for various inlet saline feed temperatures and feed flow rates for 3mm carbon-fiber spacers. The higher inlet saline feed temperature, the greater feed flow rate in the permeate flux enhancement.

The effects of the width of the S-ribs width of carbon-fiber spacer, inlet saline feed temperature, and feed flow rate on the permeate flux for both predicted and experimental
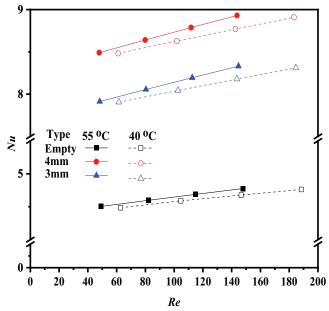
results are illustrated by Fig. 13. A higher hot feed flow rate gives higher permeate flux because the higher flow velocity mitigates the heat transfer resistance on the thermal boundary layer. The channel with S-rib carbon-fiber spacers lessens heat transfer resistance further than that of the empty channel design. Therefore, it gives more permeate flux than that of the empty channel. The fair consistency between the predicted and experimental results provides evidence-based validation that the proposed model can be used to help improve the module design and optimize the DUAGMD system's operational parameters.

In contrast to the negative effect of inlet saline feed temperature on thermal efficiency, the higher saline feed temperature in more permeate flux was observed in Table 2. Notice that a more permeate flux increment was observed for the higher hot feed temperature of 55°C than that of 40°C. Although the higher saline feed temperature encounters more heat transfer resistance than the lower saline feed temperature, more permeate flux is produced as the higher saline feed temperature gives more saturated vapor pressure gradient between both sides of the membrane. Hence, there is a need to optimally balance between the permeate flux increment gain and the thermal efficiency loss for the module design and operational parameters.

The power consumption increment is accompanied by the permeate flux enhancement due to the augmented turbulent intensity with more friction losses in the module inserted S-ribs carbon-fiber spacers set into the flow channel. Therefore, the ratio of power consumption increment to the permeate flux enhancement was presented in Fig. 14 to make suitable selections of operation and design parameters. It also assessed an optimal operation of considering economic feasibility. The effect of hot feed saline flow rate, temperature, and channel design on I_N/I_P are shown in Fig. 14. The increase of hot feed flow rate gives

Table 2
Effects of channel design and operation conditions on permeate flux N'' and flux increment I_N, $T_{c,in}$ = 25°C

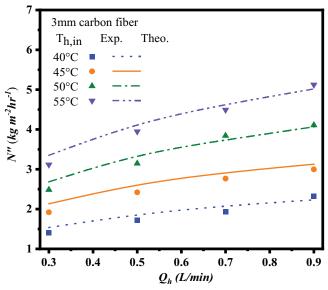| $T_{h,in}$ (°C)	Q_h (L/min)	Empty	3 mm		4 mm		5 mm	
		N''_{empty}	$N''_{s,theo}$	I_N	$N''_{s,theo}$	I_N	$N''_{s,theo}$	I_N
		(kg/(m²h))	(kg/(m²h))	(%)	(kg/(m²h))	(%)	(kg/(m²h))	(%)
40	0.3	1.418	1.538	8.46	1.524	7.48	1.513	6.70
	0.5	1.694	1.869	10.3	1.846	8.97	1.832	8.15
	0.7	1.874	2.084	11.2	2.063	10.1	2.049	9.34
	0.9	1.971	2.230	13.1	2.195	11.4	2.177	10.5
45	0.3	1.942	2.132	9.78	2.098	8.03	2.082	7.21
	0.5	2.378	2.638	10.9	2.594	9.08	2.578	8.41
	0.7	2.598	2.920	12.4	2.874	10.6	2.848	9.62
	0.9	2.728	3.128	14.7	3.078	12.8	3.040	11.4
50	0.3	2.435	2.684	10.2	2.656	9.08	2.624	7.76
	0.5	3.027	3.381	11.7	3.325	9.84	3.290	8.69
	0.7	3.301	3.738	13.2	3.689	11.8	3.645	10.4
	0.9	3.512	4.065	15.8	3.998	13.8	3.943	12.3
55	0.3	2.993	3.352	12.0	3.317	10.8	3.283	9.69
	0.5	3.689	4.169	13.0	4.122	11.7	4.079	10.6
	0.7	4.035	4.634	14.9	4.571	13.3	4.524	12.1
	0.9	4.296	5.018	16.8	4.954	15.3	4.896	14.0

Fig. 12. Effect of saline feed temperature and feed flow rate on permeate fluxes for the module with 3 mm S-ribs carbon-fiber spacers.
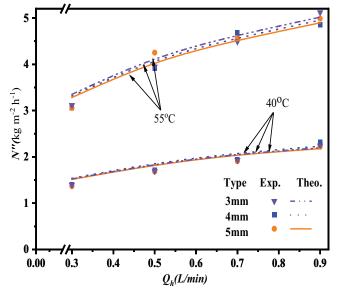

Fig. 13. Effect of the S-ribs carbon-fiber width, saline feed temperature and feed flow rate on permeate fluxes.

higher value of I_N/I_P, which means the expenses of power consumption is more effective in increasing the permeate flux. The I_N/I_P of the channel with 3mm S-ribs carbon-fiber width is higher than that of the channel with 4mm width for both saline hot feed temperature of 40°C and 55°C. Although the Nusselt number of the channel with

4mm S-ribs carbon-fiber filled channel is higher than that of 3mm width, the power consumption of the 4 mm S-ribs width is less than that of 3 mm S-ribs width. The effective utilization of power consumption, denoted by I_N/I_P, is higher if the 3 mm S-ribs carbon-fiber filled channel design is used.
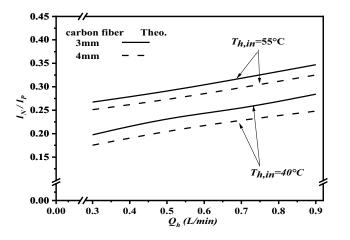
Fig. 14. Effect of saline feed flow rate, temperature and channel designs on the energy utility effectiveness.

5. Conclusions

An innovative double-unit AGMD module (DUAGMD) was devised for a high production rate with twofold permeating membrane area in a compact desalination equipment. The heat and mass transport models were established and validated for the DUAGMD to help predict the effect of inlet hot feed saline temperature, feed flow rate, and module channel design in permeate flux enhancement. The S-ribs carbon-fiber filled channel of 3, 4, and 5 mm spacer width can provide a relative increase of permeate flux of 8.46%–16.8%, 7.5%–15.3%, and 6.7%–14%, respectively. This study concludes that both the higher saline feed flow rate and feed temperature give the higher permeate flux, while the increase in feed flow rate has higher energy efficiency than the rise in hot feed temperature. Correlations of a theoretical Nusselt number for empty channel and channels with S-ribs carbon-fiber spacers were confirmed by the experimental results. These correlations and the theoretical model are helpful for the design of the DUAGMD for desalination applications. The channel design using 3mm S-ribs carbon-fiber width gives the higher permeate flux and the more efficient power utilization than the one with 4mm width. In this study, only the effects of the S-ribs carbon-fiber spacers on permeate flux performance and power consumption increment were presented. The alternative materials of the membrane, the possibility of scaling on the membrane, and the high-than-normal feed flow rate that induces wetted pore in the membrane are worth further investigation.

Symbols

A	—	Cross-sectional area of flow channel
a_w	—	Water activity in NaCl solution
C	—	Friction losses coefficient in Eq. (37)
c_k	—	Membrane coefficient based on the Knudsen diffusion model, kg m^{-2} Pa^{-1} s^{-1}
c_m	—	Membrane permeation coefficient, kg m^{-2} Pa^{-1} s^{-1}
C_P	—	Heat capacity, J kg^{-1} K^{-1}
d	—	Channel height, m
D_1	—	Carbon-fiber height, m
De	—	Equivalent hydraulic diameter of channel, m
f_F	—	Friction factor
P	—	Hydraulic dissipate energy, W
I_N	—	Permeate flux relative factor, defined by Eq. (38)
I_P	—	Power consumption relative index, defined by Eq. (39)
k_g	—	Thermal conductivity of gas, Js^{-1} m^{-1} K^{-1}
k_m	—	Thermal conductivity of membrane, Js^{-1} m^{-1} K^{-1}
k_s	—	Thermal conductivity of solid membrane, Js^{-1} m^{-1} K^{-1}
L	—	Channel length, m
ℓw_f	—	Friction loss, J kg^{-1}
M_w	—	Molecular weight of water, kg mol^{-1}
$\dot{m}$	—	Mass flow rate, kg s^{-1}
N_1	—	Number of carbon-fiber spacers
N''	—	Distillate flux, kg m^{-2} s
$\overline{N''}$	—	Average distillate flux, kg m^{-2} s
n_{step}	—	Total number of iterations
Nu	—	Nusselt number
P_m	—	Mean saturated pressure in membrane, Pa
P^{sat}	—	Saturation vapor pressure, Pa
Q	—	Volumetric flow rate, L min^{-1}
q''	—	Heat flux J m^{-2} s^{-1}
R	—	Gas constant, J mol^{-2} K^{-1}
Re	—	Reynolds number
r_p	—	Membrane pore radius, m
$S_{N''}$	—	Precision index of an experimental measurements of permeate flux, kg m^{-2} s^{-1}
$S_{\overline{N''}}$	—	Mean value of $S_{\overline{N''}}$, kg m^{-2} s^{-1}
T	—	Temperature, °C
T_m	—	Mean temperature in membrane, °C
τ_{temp}	—	Temperature polarization coefficient
$\overline{v}$	—	Average velocity, m s^{-1}
W	—	Width of channel, m
W_1	—	Carbon-fiber width, m
x_w	—	Liquid mole fraction of water
x_{NaCl}	—	Mole fraction of NaCl in saline solution
y_w	—	Vapor mole fraction of water
z	—	Axial coordinate along the flow direction, m

Greek

α	—	Aspect ratio of the channel
δ_m	—	Thickness of membrane, m
ε	—	Membrane porosity
η_v	—	Gas viscosity, Ns m^{-2}
λ	—	Latent heat of water, J kg^{-1}
μ	—	Viscosity, Ns m^{-2}
ρ	—	Density, kg m^{-3}
τ	—	Membrane tortuosity

Subscripts

1	—	Membrane surface on hot fluid side
2	—	Membrane surface on cold fluid side
c	—	Cold fluid
f	—	Reference scale

h	—	Hot fluid
empty	—	Empty channel
exp	—	Experimental results
in	—	Inlet
lam	—	Laminar
n	—	Iteration number
out	—	Outlet
s	—	Inserting carbon-fiber spacers as supporters
theo	—	Theoretical predictions

Acknowledgement

References

[1] E. Drioli, A. Ali, F Macedonio, Membrane distillation: recent developments and perspectives, Desalination, 356 (2015) 56–84.

[2] A. Alkhudhiri, N. Darwish, N. Hilal, Membrane distillation: a comprehensive review, Desalination, 287 (2012) 2–18.

[3] P. Wang, T.S. Chung, Recent advances in membrane distillation processes: membrane development, configuration design and application exploring, J. Membr. Sci., 474 (2015) 39–56.

[4] K.W. Lawson, D.R. Lloyd, Membrane distillation, J. Membr. Sci., 120 (1996) 123–133.

[5] A.M. Alklaibi, N. Lior, Membrane-distillation desalination: status and potential, J. Membr. Sci., 171 (2004) 111–131.

[6] S.O. Olatunji, L.M. Camacho, Heat and mass transport in modeling membrane distillation configuration: a review, Frontier Energy Res., 6 (2018) 130.

[7] H. Chang, J.A. Hsu, C.L. Chang, C.D. Ho, T.W. Chen, Simulation study of transfer characteristics for spacer-filled membrane distillation desalination modules, Appl. Energy, 185 (2017) 2045–2057.

[8] J. Phattaranawik, R. Jiraratananon, G.A. Fane, Heat transport and membrane distillation coefficients in direct contact membrane distillation, J. Membr. Sci., 212 (2003) 177–193.

[9] C.D. Ho, H. Chang, C.L. Chang, C.H. Huang, Theoretical and experimental studies of performance enhancement with roughened surface in direct contact membrane distillation desalination, J. Membr. Sci., 433 (2013) 160–166.

[10] X. Yang, H. Yu, R. Wang, A.G. Fane, Analysis of the effect of turbulence promoters in hollow fiber membrane distillation modules by computational fluid dynamic (CFD) simulations, J. Membr. Sci., 415–416 (2012) 758–769.

[11] M. Shakaib, S.F. Hasani, I. Ahmed, R.M. Yunus, A CFD study on the effect of spacer orientation on temperature polarization in membrane distillation modules, Desalination, 284 (2012) 332–340.

[12] Y. Dong, X.D. Dai, L. Zhao, L. Gao, Z. Xie, J.H. Zhang, Review of transport phenomena and popular Modelling approaches in membrane distillation, Membranes, 11 (2021) 122–148.

[13] K. Zhao, W. Heinzl, M. Wenzel, S. Büttner, F. Bollen, G. Lange, S. Heinzl, N. Sarda, Experimental study of the memsys vacuum-multi-effect-membrane-distillation (V-MEMD) module, Desalination, 323 (2013) 150–160.

[14] J.H. Hanemaaijer, MemstillsÒ – low cost membrane distillation technology for seawater desalination, Desalination, 168 (2004) 355–356.

[15] H. Geng, H. Wu, P. Li, Q. He, Study on a new air-gap membrane distillation module for distillation, Desalination, 334 (2014) 29–38.

[16] D. Singh, K.K. Sirkar, Desalination by air gap membrane distillation using a two hollow-fiber-set membrane module, J. Membr. Sci., 421–422 (2012) 172–179.

[17] A.E. Khalifa, S.M. Alawad, Air gap and water gap multistage membrane distillation for water desalination, Desalination, 437 (2018) 175–183.

[18] A. Omar, A. Nashed, R. Taylor, Single vs. Multi-Stage Vacuum Membrane Distillation: An Energetic Analysis, Proceedings of the 11th Australasian Heat and Mass Transfer Conference 2018, AHMTC 11, Melbourne, Australia, 2018.

[19] A.R. Da Costa, A.G. Fane, D.E. Wiley, Spacer characterization and pressure drop modelling in spacer-filled channels for ultrafiltration, J. Membr. Sci., 87 (1994) 79–98.

[20] C.D. Ho, L. Chen, K.Y. Wu, C.H. Ni, T.L. Chew, Permeate flux enhancement with a helical wired concentric tube in air gap membrane distillation systems, Desal. Water Treat.t, 202 (2020) 150–168.

[21] K.W. Lawson, D.R. Lloyd, Membrane distillation, J. Membr. Sci., 124 (1997) 1–25.

[22] R.W. Schofield, A.G. Fane, C.J.D. Fell, Gas and vapor transport through microporous membranes. I. Knudsen-Poiseuille transition, J. Membr. Sci., 53 (1990) 159–171.

[23] S.B. Iversen, V.K. Bhatia, K. Dam-Jphasen, G. Jonsson, Characterization of microporous membranes for use in membrane contactors, J. Membr. Sci., 130 (1997) 205–217.

[24] G.L. Liu, C. Zhu, C.S. Cheung, C.W. Leung, Theoretical and experimental studies on air gap membrane distillation, Heat Mass Transfer, 34 (1998) 329–335.

[25] F.A. Banat, J. Simandl, Membrane distillation for dilute ethanol separation from aqueous streams, J. Membr. Sci., 163 (1999) 333–348.

[26] S.B. Warner, Fiber Science, Princeton-Hall, Englewood Cliffs, NJ, 1995.

[27] J. Phattaranawik, R. Jiraratananon, A.G. Fane, Effects of net-type spacers on heat and mass transfer in direct contact membrane distillation and comparison with ultrafiltration studies, J. Membr. Sci., 217 (2003) 193–206.

[28] J.R. Welty, C.E. Wick, R.E. Wilson, Fundamentals of Momentum, Heat and Mass Transfer, 3th ed., John Wiley & Sons, New York, 1984.

[29] S. Kakac, R.K. Shah, W. Aung, Handbook of Single-Phase Convective Heat Transfer, Wiley, New York, 1987.

[30] R.J. Moffat, Describing the uncertainties in experimental results, Exp. Thermal Fluid Sci., 1 (1988) 3–17.